Low Work Function Lacunary Polyoxometalates as Electron Transport Interlayers for Inverted Polymer Solar Cells of Improved Efficiency and Stability

Postprint of Appl. Mater. Interfaces 9, 22773 (2017)

Lacunary Polyoxometalates Electron Transport Interlayers For Improved Efficiency and Stability of Inverted Polymers Solar Cells

Marinos Tountas,[1] Yasemin Topal,[2] Ermioni Polydorou,[1,3] Anastasia Soultati,[1] Apostolos Verykios,[1,3] Andreas Kaltzoglou,[1] Theodoros A. Papadopoulos,[4] Florian Auras,[5] Konstantinos Seintis,[3] Mihalis Fakis,[3] Leonidas C. Palilis,[3] Dimitrios Tsikritzis,[6] Stella Kennou,[6] Matroni Koutsoureli,[7] Georgios Papaioannou,[7] Mustafa Ersöz[2], Mahmut Kus,[2] Polycarpos Falaras,[1] Dimitrios Davazoglou,[1] Panagiotis Argitis,[1] Maria Vasilopoulou[1,*]

[1]*Institute of Nanoscience and Nanotechnology, National Center for Scientific Research Demokritos, 15310, Agia Paraskevi, Attiki, Greece*
[2]*Selcuk University Advanced Technology Research and Application Center, Konya, Turkey*
[3]*Department of Physics, University of Patras, 26504 Patras, Greece*
[4]*Department of Natural Sciences, University of Chester, Thornton Science Park, CH2 4NU, Chester, U. K.*
[5]*Department of Chemistry and Center for Nanoscience (CeNS) University of Munich (LMU) 81377 Munich, Germany*
[6]*Department of Chemical Engineering, University of Patras, 26504 Patras, Greece*
[7]*Solid State Physics Section, Physics Department, University of Athens, Panepistimioupolis, Zografos, Athens, Greece*
*email: m.vasilopoulou@inn.demokritos.gr

Keywords: Polymer solar cells, lacunary, polyoxometalates, titanium oxide, stability, electron transport interlayers.

Abstract

Effective material-interface engineering has been shown to play a vital role in facilitating efficient charge carrier transport, thus boosting the performance of organic photovoltaic devices. Here we employ water soluble lacunary polyoxometalates (POMs) as interlayers between the titanium dioxide (TiO_2) electron extraction layer and the organic photoactive film to simultaneously enhance the efficiency, lifetime and photostability of polymer solar cells. A significant reduction in work function (W_F) of TiO_2 upon POM insertion was observed, with the magnitude being controlled by either the amount of negative charge of the anion or by the selection of the addenda atom (W or Mo). By inserting a POM interlayer with ~10 nm thickness into the device structure, a significant improvement of the power conversion efficiency was obtained; the optimized POM-modified PTB7:PC_{70}BM-based (poly[[4,8-bis[(2-ethylhexyl)oxy]benzo[1,2-b:4,5-b′]dithiophene-2,6-diyl][3-fluoro-2-[(2-ethylhexyl) carbonyl] thieno[3,4-b] thiophenediyl]]:[6,6]-phenyl-C_{70}butyric acid methyl ester) polymer solar cells exhibited efficiency of 8.32%, which represents a 25% efficiency enhancement over the conventional architecture. Similar results were obtained in devices based on poly(3-hexylthiophene) (P3HT) with electron acceptors of different energy levels, such as PC_{70}BM or indene-C_{60} bisadduct (IC_{60}BA), which enhanced their efficiency up to 4.34% and 6.21% respectively, when using POM interlayers; this represents a 25-33% improvement as compared to the reference cells. Importantly, prolonged lifetime under ambient air and improved photostability under constant illumination was observed in POM modified devices. Detailed analysis shows that the performance and stability enhancement stem from (i) the reduced work function of TiO_2 upon POM coverage, (ii) the improved nanomorphology of the photoactive blend, (iii) the reduced recombination losses, and (iv) the superior electron transfer and exciton dissociation at the photoactive layer/POM/ TiO_2 interfaces.

1. Introduction

The low energy density of solar illumination necessitates deployment of solar technologies over large surface areas in order to capture enough of the sun's energy to offset a significant portion of non-renewable energy consumption. Polymer solar cells (PSCs) based on blends of conjugated polymer donors and fullerene acceptors, have attracted considerable interest in the field of renewable energy for both fundamental and technology-driven research.[1] Due to the enhanced understanding of fundamental photovoltaic processes in organic electronic materials, gained in recent years, as well as the constant development of new tailored materials and improved device architectures, a rapid increase of over 10% in power conversion efficiency (PCE) has been achieved in state-of-the-art single-junction devices;[2,3] this technological advancement has attracted tremendous commercial interest for further development of modern optoelectronics applications. A key issue to overcome, however, in order for PSCs to enter the market is not just to enhance their efficiency, but also (i) to increase their lifetime under ambient air and, (ii) to improve their photostability under constant

illumination. In this regard, various strategies currently exist in the phase of exploration at different levels of maturity. Among them, the well-known concept of interface engineering is one of the most promising approaches to tackle interfacial losses and improve device performance and stability.[4] In particular, the interface between the active layer and cathode electrode plays a key role in the performance of PSCs due to its fundamental importance to the electron extraction/collection process.[5-7]

Titanium dioxide (TiO_2) is a well-known electron extraction material, owing to its easy solution processability, low toxicity and high transparency across the entire visible spectral range.[8,9] However, the work function of pristine TiO_2 (~4.4-4.5 eV) is higher than the lowest unoccupied molecular orbital (LUMO) of fullerene acceptors used in photoactive blends thus hindering the extraction efficiency of photogenerated charges. Doping the TiO_2 with metallic nanoparticles, such as Ag, Zn and Sn[10,11] as well as nitrogen,[12] cesium,[13] and fluorine anions[14] could be a promising approach to improve the energetics and overall surface (and bulk) properties of TiO_2 and enhance the electron extraction/collection efficiency. Additionally, modification of TiO_2 with quantum dots,[15] self-assembled monolayers (SAMs),[16] fullerene,[17] polyethylene oxide (PEO),[18] and polyethylenimine (PEI),[19] has recently emerged as a beneficial approach for the fabrication of high efficiency PSCs. Alternatively, the surface properties of TiO_2 and the performance of fabricated PSCs are significantly improved by exposure to ultraviolet (UV) light, via the so-called "light-soaking" approach.[20-25]

Polyoxometalates (POMs), on the other hand, are a large family of inorganic early-transition metal-oxygen-anion nanoclusters with fairly rigid cage-like structures synthesized with conventional or the soft synthesis method.[26,27] They possess desired properties, such as high solubility in water-alcoholic solvents, high transparency in the visible region and adequate electron mobility, which contribute to their outstanding versatility in research areas including catalysis, energy conversion and molecular electronics.[28-30] Previously, POMs exhibiting either the Keggin or the Dawson structure were used as hole or electron injection/extraction layers, depending on their electronic properties.[31-37] In addition, our group recently demonstrated the successful application of lacunary Keggin POMs, in particular the potassium sodium 11-tungstenphosphate (α-$K_{7-x}Na_xPW_{11}O_{39}\cdot 14H_2O$, termed as B1-W) and the potassium sodium 11-molybdophosphate (α-$K_{7-x}Na_xPMo_{11}O_{39}\cdot 14H_2O$, termed as B1-Mo), as electron injection materials in fluorescent and phosphorescent organic light emitting diodes (OLEDs).[38] These lacunary POMs exhibit a significant negative charge (equal to -7) due to the absence of one $M(W,Mo)O_6$ octahedron from their structure and were found to exhibit exceptionally high electron mobility, up to 10^{-2} $cm^2\,V^{-1}\,s^{-1}$, which improved the OLED performance.[38] In this work, the lacunary POMs under study, as well as the newly introduced potassium 9-tungstenphosphate (α-$K_9PW_9O_{34}\cdot 16H_2O$, termed as B2-W), the structure of which exhibits three WO_6-octahedrals less, promoting a higher negative charge (equal to -9), are inserted as effective interlayers between the TiO_2 electron extraction layer and the photoactive film in PSC inverted architectures. Moreover, the high electron mobility of these lacunary structures is expected to be beneficial for electron transport as compared to other commonly used materials such as SAMs, PEI, PEO and quantum dots, which are rather insulating in nature. We find that the insertion of POM interlayers results in (i) significant reduction in the W_F of TiO_2 thus enhancing the electron extraction/collection efficiency, (ii) reduced recombination losses, (iii) improved nanomorphology of the photoactive blend, (iv) superior electron transfer, and (v) more effective exciton dissociation at the photoactive-layer/POM/TiO_2 interface. As a consequence, the insertion of POM interlayers significantly improved the performance and boosted the lifetime, under ambient air, and photostability of PSCs based on different donor:acceptor combinations.

2. Results and discussion

2.1 Optoelectronic properties and surface morphology of TiO_2/POMs. The chemical structures of lacunary POMs used in this study are shown in Figure 1a. B1-W and B2-W contain WO_3 units while B1-Mo consists of MoO_3 units as shown in Fourier-transform IR (FTIR) spectra presented in Supporting Information (Figures S1-S3). The transmittance spectra of TiO_2 films on glass substrates before and after coverage with a ~10 nm POM film (spin coated from water solutions with a concentration of 10 mg/ml) are shown in Figure 1b. No obvious changes of TiO_2 upon POM coating is observed, which is beneficial for device performance since the light passes through the cathode/TiO_2/POM interfaces to enter into the device. Note that the absorption spectra and bandgap of TiO_2 films also remained unaffected upon POMs deposition on TiO_2. (Figure S4). The coverage of TiO_2 film with POM was also studied since it affects interfacial contact, which is a key factor governing the solar cell performance. Atomic force microscopy (AFM) was used to investigate in detail the

influence of POM interlayers on the morphology of TiO_2 substrate. As seen in Figure 1c, pristine TiO_2 film has a relatively smooth surface with a root-mean-square (RMS) of 2.84 nm. Upon coating B1-W and B2-W layers, the TiO_2/POM films show a slightly increased RMS roughness of 3.56 and 4.51 nm (Figures 1d, 1e) whereas in the case of TiO_2/B1-Mo bilayer the RMS roughness remains nearly similar to that of TiO_2 (2.90 nm). The small deviations in roughness are not expected to significantly alter the physical contact between cathode interlayer and organic film thus affecting the device performance. We further evaluated the POM coverage of TiO_2 layers via X-ray photoelectron spectroscopy (XPS). Figures 2a, 2b and 2c present the W4f and Mo3d peaks of XPS spectra taken on B1-W, B2-W and B1-Mo, respectively, coated on TiO_2 substrates. These peaks reveal a small reduction (under-stoichiometry) of POMs, as concluded from the appearance of doublets attributed to lower oxidation states of the metals of MO_3 units (except of W^{6+} and Mo^{6+} states a small contribution from W^{5+} and Mo^{5+} is evident). The reduction of POMs has previously been considered to be the source of improved electron transport and increased electron mobility of these materials.[33]

In addition, as the W_F of the interlayer is of significant importance for the device performance, ultraviolet photoelectron spectroscopy (UPS) was used to test the electronic properties of various POM interlayers on TiO_2 substrates (Figure 2d). TiO_2 film possesses a typical W_F of 4.5 eV (Figure 2e) which decreases to 4.2, 4.0 and 3.8 eV upon its coverage with B1-W, B2-W and B1-Mo, respectively. The decrease in the W_F of POM modified TiO_2 was also supported by measurements of the contact potential difference (CPD) of bare and POM coated TiO_2 samples using the Kelvin probe technique (Figure 2f). A pronounced decrease of the CPD of TiO_2 was observed upon POM coating. In particular, the CPD with respect to TiO_2 was -0.43 V, -0.50 V and -0.65 V for B1-W, B2-W and B1-Mo modified TiO_2 layers, respectively, following the same trend as the reduction in W_F values measured with UPS. The lower W_F of TiO_2/POM samples is expected to allow the formation of ohmic contacts with fullerene acceptors and to increase the built-in voltage of the solar cell, which is beneficial for electron extraction while also suppressing recombination losses.[39-41] Note that larger reduction of TiO_2 W_F was caused using POMs having either Mo as addenda and the same charge (B1-Mo as compared with B1-W) or the same addenda but higher negative charge (B2-W as compared to B1-W).

To explain the origin of the W_F shift upon TiO_2 coverage with POMs, we also carried out theoretical calculations via density functional theory (DFT), following the procedure described in the methodology section. It is well known that oxygen vacancies are always present on the surface of TiO_2 (101).[8] There are three possible oxygen vacancies on the TiO_x(101) surface,[8] for which the total density of states (DOS) is shown in Figure 2g. We observe that all three surface O vacancies provide energy states appearing below the conduction band minimum (CBM) just below the Fermi level (0.0 eV). All three vacancy types display major contribution from Ti 3*d* states with a minimal hybridization from O 2*p* states at an energy range within -0.4 eV below the Fermi level. Similar results were also obtained when calculating the DOS for TiO_x (100) (Figure S5) and TiO_x (001) (Figure S6) surfaces. In order to investigate the possible interaction of POMs with TiO_x, we studied the electronic structure of the three aforementioned POM materials. After geometry optimization was performed on the isolated B1 structures (Figure S7), we observed that two oxygen atoms have the tendency to withdraw from both structures, making B1-W and B1-Mo under-stoichiometric, as also demonstrated by XPS measurements (Figure 2 a-c). The calculated dissociation energy of the two oxygen atoms was found to be -0.16 eV indicating that their adsorption on the TiO_x surface is possible. Figure 2h shows the total DOS of the under-stoichiometric B1-W, which displays sharp states in the middle of the band gap contributed by O 2*p* orbitals. The fact that the Fermi level is not aligned to the oxygen gap states of TiO_x is expected not to be beneficial in terms of efficient charge transfer between B1-W and metal-oxide, which is confirmed by the moderate decrease in the W_F of the latter. On the other hand, B2-W and B1-Mo (Figures 2i, and 2j) show the appearance of a range of states in the band-gap close to the Fermi level, all related to O 2*p* orbitals. This provides an indication of effective energy level alignment between the metal-oxide surface and the B2-W and B1-Mo structures,[42] thus favoring electron transfer from the POM adsorbates to the TiO_2 substrate. The latter has a net downward shift of the vacuum level causing the reduction in W_F of the POM-modified TiO_2 surface, as observed experimentally.

2.2 Polymer solar cells performance. To unravel the effect of POM interlayers on PSCs performance we fabricated devices of inverted configuration (Figure 3a) using pristine or POM modified TiO_2 electron transport/extraction layers. In order to explore the universal applicability of POMs we used photoactive blends consisted of combinations of two different polymer donors and two fullerene acceptors, namely

P3HT:$PC_{70}BM$, P3HT:$IC_{60}BA$ and PTB7:$PC_{70}BM$ (Figure 3a). The corresponding energy level diagram is shown in Figure 3b. For completeness, we also show the energy levels of the MoO_x/Al hole collection anode electrode. It is observed that upon POM coverage of TiO_2, its W_F reduces thus decreasing the band offset and improving the energetic alignment with the LUMO of $PC_{70}BM$ and $IC_{60}BA$, resulting in the formation of an interface that provides barrier-free electron transport. Moreover, the insertion of POM interlayer causes the formation of an interfacial dipole between the active layer and the cathode interface with the negative pole of this dipole pointing from the POM surface towards TiO_2. Such favorable dipole further enhances electron transport under short circuit conditions. At the same time, because the cascade energy structure for electron extraction between the cathode interface and organic semiconductor is largely improved, one can expect a faster charge sweeping-out and, thus, a higher short circuit photocurrent combined with an increased open circuit voltage upon POM coating of TiO_2.

At first, P3HT:$PC_{70}BM$-based PSCs using different thicknesses of POM films were fabricated. The variation of PCE of these devices versus POM thicknesses is shown in Figure S8a. Although the cell performance was relatively insensitive for POM thicknesses between 5 and 30 nm, probably due to the high electron mobility of these POMs in the solid state,[38] it exhibited a maximum value for a POM thickness around 10 nm. Note that the slopes of current-voltage characteristics of electron-only devices with the structure FTO/TiO_2/POM/Al were slightly higher as compared with the device without the POM interlayer (Figure S8b), which highlights the conducting nature of POMs. Figure 4a plots the current density-voltage (J-V) characteristics of the best performing P3HT:$PC_{70}BM$-based devices that consisted of 10 nm thick POM covered TiO_2 layers under simulated A.M. 1.5 illumination (100 mW/cm^2). The corresponding dark J-V curves are shown in Figure 4b. Table 1 presents the overall photovoltaic performance of these devices. After coating a POM interfacial layer on the TiO_2 surface, the devices exhibited increased short-circuit current (J_{sc}), open-circuit voltage (V_{oc}) and fill factor (FF) values starting from 9.40 mA cm^{-2}, 0.60 V and 0.58, respectively, for the device with bare TiO_2 (which exhibited a PCE of 3.27%) and reaching 10.60 mA cm^{-2}, 0.63 V and 0.65, respectively, for the B1-Mo covered TiO_2-based device. Although the device using the TiO_2 layer covered with the B1-Mo POM demonstrates the best performance, yielding a PCE of 4.34%, representing a 33% improvement as compared with the control device, PSCs with B1-W and, especially, with B2-W interlayers are also of high performance. The increase in the FF and the carrier collection efficiency are attributed to the decrease of the series R_s and the increase of the shunt resistance R_{sh} of the devices upon the insertion of POM interlayer. These are further supported by the suppression of the dark reverse saturation current and the increase of the forward current (above turn-on voltage) of the POM modified devices, as evidenced by the dark J-V characteristics. Additionally, the observed increase in V_{oc} could be ascribed to the improved interfacial energetic alignment and reduced recombination losses since both these fundamental processes affect V_{oc}.[43-45] Figure 4c shows the corresponding external quantum efficiency (EQE) of these devices before and after the insertion of POM interfacial layers. EQE spectra with a similar shape are obtained from these devices, with no contribution beyond the absorption edge of P3HT,[46] consistent with the negligible optical density of interfacial layers of these molecules in relation to that of P3HT. This result indicates that these POM molecules only modify the interface rather than harvest light.

To investigate the potential universal applicability of POM interlayers, we next fabricated PSCs based on blends of the same donor with a different acceptor (P3HT:$IC_{60}BA$) and of the same acceptor with a different donor (PTB7:$PC_{70}BM$). The J-V curves for the P3HT:$IC_{60}BA$-based PSCs measured under 1.5 AM illumination are presented in Figure 4d, the dark J-V curves of the same devices are shown in Figure 4e, and the corresponding EQE spectra are provided in Figure 4f. The J_{sc}, V_{oc}, FF and PCE values are summarized in Table 1. The P3HT:$IC_{60}BA$-based devices with bare TiO_2 layer exhibited a PCE of 4.95%, with a J_{sc} of 9.90 mA cm^{-2}, a V_{oc} of 0.77 V and a FF of 0.65. After a thin interlayer of B1-W or B2-W with an optimized thickness of 10 nm was inserted into the device structure, the PCE reached 5.74% and 6.01%, respectively. A device with a 10 nm thin B1-Mo interlayer exhibited an even higher average PCE of 6.21%, as derived from measured J_{sc} of 10.80 mA cm^{-2}, V_{oc} of 0.81 and FF of 0.71, representing a 25% improvement as compared with the reference device. Improved performance was also obtained in PTB7:$PC_{70}BM$-based devices upon POM coverage of TiO_2 (Figures 4g). The significant improvement in FF, J_{sc} and V_{oc} of the POM incorporated cells yielded PCEs of 7.45% and 8.15% in TiO_2/B1-W and TiO_2/B2-W based devices and of 8.32% in the TiO_2/B1-Mo device; the latter represents a 25% improvement as compared with the reference cell (6.55%). The lower contact resistance, better rectification ratio (lower leakage current) (Figure 4h), and improved

photon-to-electron conversion efficiency (Figure 4i), were again verified in the POM modified PTB7:$PC_{70}BM$-based cells. Notably, improved performance when inserting POM interlayers was also obtained in PSC devices using poly[N-9'-heptadecanyl-2,7-carbazole-alt-5,5-(4',7'-di-2-thienyl-2',1',3'-benzothiadiazole)] (PCDTBT) as the polymer donor blended with $PC_{70}BM$ acceptor (Figure S9, Table S1), thus further demonstrating the universality of our approach.

2.3 Additional device characterization, photophysical properties of photoactive polymers and nanoscale morphology of photoactive blends on TiO_2/POM layers. The largely improved photocurrent measured in the POM modified devices could be explained through better selectivity of the cathode interface which was further verified by J-V measurements taken in electron-only devices. These devices exhibited the following structure: FTO/TiO_2/POM/photoactive blend/Al, where the photoactive blends consisted of either P3HT:$PC_{70}BM$ or P3HT:$IC_{60}BA$ or PTB7:$PC_{70}BM$, while the MoO_x/Al hole selective contact was replaced by Al. The J-V characteristics are shown in semi-logarithmic plots in Figure 5a, 5b and 5c, respectively. A substantial increase in electron current is observed in three types of devices upon the insertion of POM interlayers. This improvement in electron current density can be attributed to the significant decrease of the W_F of TiO_2 layer upon POM coating and the high electron mobility of POMs.

Next, the variation of V_{oc} of P3HT:$PC_{70}BM$ (Figure 5d), P3HT:$IC_{60}BA$ (Figure 5e) and PTB7:$PC_{70}BM$ (Figure 5f) based devices under 1.5 AM illumination with different light intensities was probed. We find that all type of reference devices exhibit slopes higher than KT/q (1.61 KT/q, 1.42 KT/q and 1.39 KT/q, respectively) indicating a strong dependence on light intensity. These relatively high slopes indicate an increased number of electron trapping sites and a, concomitant, large increase in the number of trap assisted Shockley-Read-Hall (SRH) monomolecular recombination processes in the reference cells.[47-49] On the contrary, the slopes in the TiO_2/POM based devices are significantly lower (1.09, 1.11, 1.06 KT/q for B1-W modified devices based on P3HT:PC_{70}, P3HT:$IC_{60}BA$ and PTB7:$PC_{70}BM$, respectively, 1.07, 1.04, 1.03 KT/q for B2-W based devices and 1.06, 1.05, 1.04 KT/q for the devices using the B1-Mo interlayer). The decreased slopes indicate much lower trap assisted recombination at open circuit and an enhancement of selectivity of the POM modified cathode. The above suggest that insertion of POM interlayers at the TiO_2/organic interface facilitates the crossover from monomolecular or TiO_2 surface trap assisted to a pure bimolecular recombination process at open circuit, thus positively influencing the FF, the V_{oc} and the stability of PSCs.

Time resolved photoluminescence (TRPL) measurements were next carried out on P3HT and PTB7 films deposited on TiO_2 and TiO_2/POM substrates to elucidate the charge separation/extraction and exciton recombination dynamics at the TiO_2/POM/organic interfaces. In Figure S10a the steady-state PL spectra of ~20 nm thin P3HT film deposited on different TiO_2 layers, are presented. The characteristic emission peaks of P3HT at around 650 and 720 nm corresponding to the 0-0 transition and the 0-1 and 0-2 sidebands, as previously reported by Ruderer et al,[46] are evident. The PL spectra of P3HT on TiO_2, B1-W/TiO_2 and B2-W/TiO_2 layers have almost the same intensity while for P3HT on B1-Mo/TiO_2, the PL intensity is significantly reduced, which is an indication of the enhanced electron accepting capability of B1-Mo. Figure 5g shows the normalized transient PL decay curves obtained with a femtosecond laser of the bare P3HT and the P3HT/TiO_2 films through POM interfacial modification. We fitted the curves of P3HT films deposited on TiO_2/POM layers with a three-exponential decay function and obtained the corresponding decay lifetimes (Table 2). Notably, a two-exponential decay was found to satisfactorily describe the PL dynamics of P3HT/TiO_2 films. The third component decay time that was revealed in TiO_2/POM/P3HT bilayers is much shorter than the other two components (<1 ps) and may be ascribed to a new, efficient channel for exciton decay of P3HT on POMs followed by fast electron transfer. All TiO_2/POM/P3HT samples demonstrate efficient charge transfer at interfaces, by showing a shorter PL lifetime, τ, than pristine P3HT (17.94 ps) deposited on glass substrate (Figure S11 and Table S2). The measured PL lifetime of the P3HT on pristine TiO_2 films or covered with B1-W, B2-W and B1-Mo are 11.30 ps, 9.20 ps, 7.70 ps and 6.34 ps, respectively, representing a decrease of 36.9%, 48.6%, 60.0% and 64.8% compared to that of pristine P3HT on glass. The improved charge separation (i.e. shorter lifetime) at thin P3HT films deposited under identical conditions on different TiO_2/POM substrates implies that POM can effectively mediate charge transfer between P3HT and TiO_2, due to the significant decrease in the W_F of TiO_2 upon POM coating. However, although the POM coverage of TiO_2 granted significant quenching of steady-state PL intensity of 40 nm thick PTB7 films (Figure S10b), thus verifying the role of POMs as potential electron acceptors and charge transfer mediators, it induced smaller deviations

in exciton lifetimes as compared with P3HT as revealed from TRPL measurements using a picosecond laser upon excitation at 468 nm and detection at 790 nm (Figure 5h, Table 2). In particular, the estimated exciton lifetimes of PTB7 deposited on TiO_2 and TiO_2/B2-W were identical (0.35 ns) while a small decrease was observed in those obtained for deposition on TiO_2/B1-Mo substrate (0.33 ns) and B1-W (0.31 ns) indicating more efficient exciton dissociation in these cases. However, one should take into account that it was deemed necessary to measure exciton lifetimes in PTB7 films with larger thickness (about 40 nm) as compared with P3HT (about 20 nm), due to the lower photoluminescence quantum yield of PTB7,[50-55] which makes the direct probing of exciton decay/charge transfer phenomena occurring in inorganic substrate/organic interfaces a more difficult task. However, our findings explicitly confirmed the potential of POM interlayers in regulating the TiO_2 properties, especially in reducing its W_F and enhancing the electron transfer rates, which lead to the increased built-in electric field (or voltage) (V_{bi}) contributing to the improved V_{oc} (Table 1). At the same time the increased V_{bi} promotes the transport of the photogenerated electrons (after charge separation) towards the TiO_2 layer (Figure 5i).[56-58] This fast electron transport is considered to cause the enhancement of electron current as well as of J_{sc} of the POM modified devices.

Next, we studied the surface morphology of photoactive films on TiO_2 with and without POM interlayers, as the photovoltaic performance of PSCs is significantly affected by the morphology of the photoactive layer.[46,59,60] The surface topography was investigated only in the cases of P3HT:$PC_{60}BM$ and P3HT:$IC_{60}BA$ blends due to well-known crystallization ability of P3HT.[61] On the contrary, it was not possible to probe the nanomorphology of the PTB7:$PC_{70}BM$ system, due to poor organization of this blend.[62,63] 2D 5x5 μm atomic force microscopy (AFM) topography images are shown in Figures 6 a-d for P3HT:$PC_{70}BM$ and in Figures 6e-h for P3HT:$IC_{60}BA$ deposited on TiO_2 pristine and covered with the different POM films. It is observed that the distribution of P3HT donor and the fullerene acceptors and their interpenetrating networks are quite different when deposited on different substrates with smaller donor:acceptor domains (i.e. finer, smaller scale, phase separation) to be formed when photoactive blends are deposited on POM covered TiO_2; in particular for the P3HT:$PC_{70}BM$ blend. In addition, a small reduction in the RMS roughness of the blends deposited on TiO_2/POM layers is observed (5.11, 4.46, 4.07 nm for P3HT:$PC_{70}BM$ and 8.25, 8.23, 8.06 nm for P3HT:$IC_{60}BA$ deposited on TiO_2/B1-W, TiO_2/B2-W and TiO_2/B1-Mo, respectively) when compared with blends deposited on TiO_2 (5.52 nm and 9.91 nm, respectively). This indicates that the film formation and physical contact at the POM/photoactive layer interface is more uniform and should lead to a more uniform electrical contact, as also indicated from the reduced series resistance and increased shunt resistances of POM modified solar cells (Table 1). To explain the differences in photoactive blends nanomorphology we probed the surface wetting characteristics of TiO_2 layers before and after coating with POMs by taking contact angle measurements. As shown in Figures S12 a and b and Table S3, upon POM coating on TiO_2 smaller contact angles were obtained indicating a small increase of both hydrophilicity, as expected due to the hydrophilic nature of POMs,[64] and surface energy of the substrate. Interestingly, the spreading of the solvent (chlorobenzene) and of active layer solutions (Figure S13) was excellent for all surfaces of samples prepared in this work, which reflects the effective wetting of the POM interfacial layers with the photoactive blends, as a result of the enhanced hydrophilicities and surface energies for the POM coated TiO_2 layers.

2.4 Enhancement of stability under ambient air and photostability upon POM modification. The stability under ambient air of un-encapsulated devices using TiO_2 coated with POM interlayers was also substantially improved, as shown in Figure 7 where the variation over time of J_{sc}, V_{oc}, FF and PCE of P3HT:$IC_{60}BA$ (Figures 7 a-c) and PTB7:$PC_{70}BM$ (Figures 7 d-f) based devices is presented. The POM modified devices retained about 83-84% for P3HT:$IC_{60}BA$ and 76-77% for PTB7:$PC_{70}BM$ of their original PCE values after 400 hours. In contrast, the PCE of the reference devices degraded to almost 58% for P3HT:$IC_{60}BA$ and to 40% for PTB7:$PC_{70}BM$ under the same conditions. Note that the devices were kept in dark between measurements. Similar results were obtained for P3HT:$PC_{70}BM$ based devices (Figure S14). This significant increase in the ambient stability of devices using TiO_2/POM layers is ascribed to reduced TiO_2 electron trapping sites and concomitant surface recombination upon POM coating, to improved interfacial energy level alignment and to an overall better quality of the cathode interface (improved physical contact, enhanced electron transport characteristics, lower electron extraction barrier) and photoactive blend (improved nanomorphology).[65]

Photostability of polymer solar cells also represents a key requirement for the commercialization of this technology. A key aspect for this work was therefore to investigate if POM modification of TiO_2/photoactive blend interfaces can prevent light induced degradation. We therefore investigated the photostability of P3HT:$IC_{60}BA$ (Figures 8 a-c) and P3HT:$PC_{70}BM$ (Figure S15) based PSCs using either pristine TiO_2 or modified with POM (B2-W and B1-Mo, in particular) interlayers under 1.5 AM illumination. As shown in Figures 8 a-c, after 20 h of illumination the PCE of the P3HT:$IC_{60}BA$-based device using pristine TiO_2 layer is substantially reduced to 49% of the initial value, while a much smaller degradation is observed in similar devices upon POM modification. These devices preserve 75-77% of their initial PCE value after 20 hours of illumination. J_{sc}, decreased with a similar trend with that of PCE in those devices while V_{oc} and FF remain quite stable in the POM modified devices revealing that interfacial resistances are less affected by illumination as a result of the improved cathode interfaces in these devices.[66] On the contrary, all PTB7:$PC_{70}BM$ based devices (especially those using the pristine TiO_2 film) were rapidly degraded when illuminated with full 1.5 AM light which is in agreement with studies reported by other groups (Figures 8 d-f).[14,67] The poor device stability was previously ascribed to UV light induced oxidation of PTB7.[67] We therefore performed additional stability studies using a UV cut-off filter (UCF), which blocks UV photons with wavelengths below 405 nm. It is observed that upon using the UCF filter the reference device preserves about 57% of its initial PCE after 20 hours of illumination while those based on TiO_2/POM cathode interfaces maintain nearly 76-77% of their initial PCEs demonstrating the beneficial effect of POM interfacial layers on device photostability. This improvement, upon excluding UV light from entering the device, may be attributed to the overall (physically and energetically) improved POM-modified TiO_2/PTB7:$PC_{70}BM$ interface contact (Note that, when measured using the UV filter, the initial performances of the PTB7:$PC_{70}BM$-based devices were slightly lower than those obtained without using the filter, due to the lower light intensity). Our results demonstrate the POM interlayers provide a solution for fabricating low-cost, environmentally friendly, high performing and stable organic solar cells that is expected to be applicable to a wide range of polymer, small-molecule or perovskite-based photoactive blends.

3. Conclusions

In conclusion, we successfully demonstrated the improvement of PCE, lifetime and photostability of PSCs under constant illumination upon using water soluble lacunary POMs, with a high negative charge, as interfacial-modifying layers deposited on TiO_2. These interlayers are widely applicable in various photoactive material systems, such as PTB7:$PC_{70}BM$, P3HT:$IC_{60}BA$ and P3HT:$PC_{70}BM$. The overall improved device performance was attributed to the significant reduction of the work function of TiO_2 upon POM modification, which was found to be dependent on the absolute value of the negative charge of the POM anion as well as the addenda type. In addition, the POM-improved nanomorphology of the photoactive blend, the reduced trap assisted recombination losses and the superior electron transfer and exciton dissociation at the POM-modified TiO_2 cathode interfaces also contributed to prolonged device efficiency and improved overall stability. We anticipate that our findings will catalyze the development of novel TiO_2/POM bilayers as well as TiO_2:POM composite materials, which may play a pivotal role in the development of efficient and stable organic photovoltaic devices and perovskite solar cells.

4. Experimental section

Synthesis of lacunary POM materials. To synthesize the B1-W 50 mL of H_3PO_4 1M and 88 mL of glacial CH_3COOH were added in a solution of $Na_2WO_4{\cdot}2H_2O$ (181.5 g, 0.550 mol) in 300 mL water. The solution was refluxed during one hour and then KCl (60 g, 0.805 mol) was added; the white precipitate, which appeared, was filtered, washed with water and dried in air to afford the B1-W. Similarly, in a solution of $Na_2MO_4{\cdot}2H_2O$ (133.04 g, 0.550 mol) in 220 mL water, 36.6 mL of H_3PO_4 1M and 64.4 mL of glacial CH_3COOH were added. The solution was refluxed during 30 minutes, then KCl (43.8 g, 0.805 mol) was added; the white precipitate which appeared was filtered, washed with water and dried in air to afford the B1-Mo. For the synthesis of B2-W 60 mL of K_2CO_3 2M were added to a solution of 64 g of α-$K_{7-x}Na_xPW_{11}O_{39}{\cdot}14H_2O$ in 200 mL of water; the white precipitate which appeared was filtered, washed with alcohol and dried in air to afford B2-W.

Titanium Oxide Layer Preparation. FTO-coated glass (Pilkington TEC 15, <15 Ohms/sq) was cleaned by sonication in detergent solution (Hellmanex III, Hellma Analytics), water and ethanol, followed by treatment

in oxygen plasma for 5 min. A solution of 13 µL concentrated aqueous HCl in 5 mL of dry isopropanol was slowly added to a stirred solution of titanium isopropoxide (711 mg, 2.5 mmol) in 5 mL of dry isopropanol. The cleaned substrates were spin-coated at 2000 rpm with this titania precursor solution and immediately placed on a hotplate at 150 °C. Subsequently, the samples were then calcinated at 500 °C for 45 min (1 h ramp).

Computational methodology. Theoretical calculations for the TiO_x (101) surface, which is the most stable and exposed crystal surface of TiO_2 anatase, were carried out following the methodology published in Ref. 8. In terms of the POMs discussed in this work, all calculations were spin-polarized, performed using the Vienna Ab Initio Simulation Package (VASP). Plane-wave basis sets and the Perdew-Burke-Ernzerhof (PBE) functional was used along with the Grimme DFT-D2 method, taking into account spin-orbit coupling. Geometry optimization was carried out with maximum atomic forces set at 0.01 $e \cdot Å^{-1}$ and a Γ centered k-point grid of 1×1×1; initial crystal structures and atomic coordinates for the B1 structures were taken from work done by Mizuno et al. and for the B2 structure by Li et al.[68,69] All DOS calculations were performed via the projector augmented wave (PAW) method, with a plane-wave cut-off energy of 400 eV and a Γ centered k-point grid of 2×2×2. Gaussian smearing with a width of 0.05 eV was used to determine how partial occupancies are set for each wave-function. Finally, all POM supercells were modelled within a simple cubic cell of dimensions a=20 Å.

Device Fabrication. Polymer solar cells were fabricated on TiO_2 films with a thickness of 50 nm, which served as electron transport/extraction layers and were deposited on FTO coated glass substrates, as described above. POMs were spin coated on pre-cleaned (with a sequence of acetone, isopropanol and DI water) TiO_2 films from water solutions (solutions of B1-W and B2-W were stirred for about 2 h without heating, while for B1-Mo a short annealing step at 90 ^oC was deemed necessary in order to be fully dissolved in water) through rotation at 1000 rpm for 20 sec and, sequentially at 2000 rpm for another 20 sec. Note that we also tested POM solutions in methanol, in mixtures water:methanol (4:1, 2:1, 1:1, 1:2, 1:4), in DMSO and DMF but the best results (higher efficiencies) were obtained from water solutions. After deposition a post-annealing study of POMs was performed, which revealed that the best device efficiencies were obtained when POMs were not subjected to any post deposition annealing treatment. The active layer consisted of P3HT:$PC_{70}BM$ blend (10 mg ml^{-1} for P3HT, 8 mg ml^{-1} for $PC_{70}BM$ in 1,2 dichlorobenzene) with a thickness of 150 nm or P3HT:$IC_{60}BA$ (17 mg ml^{-1} for P3HT, 17 mg ml^{-1} for $IC_{60}BA$ in 1,2-dichlorobenzene) with a thickness of 200 nm. After spin coating (at 600 rpm for 40 sec for P3HT:$PC_{70}BM$ and at 800 rpm for 30 sec for P3HT:$IC_{60}BA$) the photoactive layers were left to dry for about 30 min and then annealed at 150 °C for 10 min. PTB7:$PC_{70}BM$ was deposited via spin coating at 1000 rpm for 90 sec from solutions with concentration 10 mg ml^{-1} for PTB7, 15 mg ml^{-1} for $PC_{70}BM$ in 1,2 dichlorobenzene where 3% per volume of DIO was added to deliver a thickness of 85 nm and then was left to dry without being subjected to any post-deposition annealing. Note that all depositions and thermal annealing treatments of P3HT:$IC_{60}BA$ and PTB7:$PC_{70}BM$ films were carried out in the inert environment of an argon filled glove-box with oxygen and humidity levels below 1.0 ppm. Then, an approximately 20 nm-thick under-stoichiometric molybdenum oxide (MoO_x) layer was deposited on top of the active layer, using a previously reported method, to serve as the hole transport/extraction material.[70] The devices were completed with a 150 nm thick aluminium anode, deposited in a dedicated thermal evaporator at a pressure of 10^{-6} Torr through a shadow-mask, which defined the device active area to be equal to 12.56 mm^2. The devices were then measured in air at room temperature without additional encapsulation.

Measurements and Instrumentation. X-ray photoelectron spectra (XPS) and Ultraviolet Photoelectron Spectra (UPS) were recorded by Leybold EA-11 electron analyzer operating in constant energy mode at pass energy of 100 eV and at a constant retard ratio of 4 eV for XPS and UPS. All binding energies were referred to the C 1s peak at 284.8 eV of surface adventitious carbon, respectively. The X-ray source for all measurements was an unmonochromatized Mg Kα line at 1253.6 eV (12 keV with 20 mA anode current). The valence band spectra of titanium oxides without and with POM interlayers were evaluated after recording the UPS spectra of about 50 nm thick films deposited on an FTO substrate. For the UPS measurements, the He I (21.22 eV) excitation line was used. A negative bias of 12.22 V was applied to the samples during UPS measurements in order to separate secondary electrons originating from sample and spectrometer and to estimate the absolute work function value from the high BE cut-off region of the UPS spectra. The analyzer resolution is determined from the width of the Au Fermi edge to be 0.16 eV. The steady state photoluminescence spectra of P3HT on various substrates were taken by means of a Fluoromax spectrometer

(Horiba) upon excitation at 530 nm. The films were placed on a specific holder for solid samples and the spectra were corrected for the sensitivity of the detector. The PL dynamics of P3HT samples were studied under magic angle conditions, by using a femtosecond upconversion technique. The excitation of the samples was realized by means of the second harmonic of a Ti:Sapphire laser at 410 nm. The average power was less than 3 mW while the repetition frequency was 80 MHz. The PL of the samples was collected and focused together with the remaining fundamental fs laser beam on a 0.5 mm BBO crystal to produce frequency mixing. A long pass filter was used to exclude scattering light from the excitation beam. The upconverted beam passed through an iris, filters and a monochromator and was detected by a photomultiplier. The Instrument's Response Function (IRF) was approximately 150 fs. A three-exponential function convoluted with the IRF was used for fitting the dynamics. The PL dynamics of PTB7 samples were studied under magic angle conditions, by using a Time Correlated Single Photon Counting (TCSPC) technique (Fluotime 200, Picoquant). The excitation of the samples was realized by means of a ps diode laser at 468 nm having a pulse duration of 80 ps. The fluorescence of the samples was collected and passed through a detection analyzer and a monochromator. It was finally detected by a micro-channel plate photomultiplier. The IRF of the TCSPC spectrometer was ~80 ps. The best fitting was achieved by a multi-exponential function convoluted with the IRF and was determined by inspection of the residuals and through the χ^2 factor which should be smaller than 1.1. EQE measurements were carried out using an Autolab PGSTAT-30 potentiostat, with a 300 W Xe lamp in combination with an Oriel 1/8 monochromator for dispersing the light in an area of 0.5 cm^2. A Thorlabs silicon photodiode was used for the calibration of the spectra. All measurements were performed in air. Absorption measurements were taken using a Perkin Elmer Lampda 40 UV/Vis spectrophotometer. FTIR transmission spectra of ZnO films were obtained on a Bruker Tensor 27 spectrometer (at 4 cm^{-1} resolution, 128 scans) with a DTGS detector. Surface morphology and structure were investigated with an NT-MDT atomic force microscope (AFM) operated in tapping mode. The thicknesses of films were measured with an Ambios XP-2 profilometer and a M2000 Woolam ellipsometer. Current density-voltage characteristics of the fabricated solar cells were measured with a Keithley 2400 source-measure unit. Cells were illuminated with a Xe lamp and an AM 1.5G filter to simulate solar light illumination conditions with an intensity of 100 mW/cm^2 (1 sun), as was recorded with a calibrated silicon photodiode. To accurately define the active area of all devices we used aperture masks during the measurements with their area equal to those of the Al contacts (12.56 mm^2).

Acknowledgements
This work was performed in the framework of "YDISE" project within GSRT's KRIPIS action, funded by Greece and the European Regional Development Fund of the European Union under NSRF 2007–2013 and the Regional Operational Program of Attica. TP acknowledges use of Hartree Centre computational resources via the 3rd BlueJoule Access Programme, under project No. HCBG125, funded by the U.K. Science and Technology Facility Council (STFC), as well as local computational facilities provided by the Faculty of Science and Engineering, University of Chester, U.K.

Supporting Information
Additional Figures (S1-S15) and Tables (S1-S3) are included in the Supporting Information: FTIR transmittance and UV-vis absorption spectra of POMs, J-V characteristics of PCDTBT:$PC_{70}BM$-based devices, contact angle measurements, steady-state and time resolved PL spectra, stability measurements of P3HT:$PC_{70}BM$ films using TiO_2 interlayers with different POM interfacial layers, atomic structure and DOS of TiO_2 surfaces, theoretical estimated POM chemical structures.

References
1. Cao, W.; Xue, J. Recent Progress in Organic Photovoltaics: Device Architecture and Optical Design. *Energy Environ. Sci*. **2014**, *7*, 2123–2144.
2. Nian, L.; Zhang, W.; Zhu, N.; Liu, L.; Xie, Z.; Wu, H.; Würthner, F.; Ma, Y. Photoconductive Cathode Interlayer for Highly Efficient Inverted Polymer Solar Cells. *J. Am. Chem. Soc.* **2015**, *137*, 6995–6998.
3. He, Z.; Xiao, B.; Liu, F.; Wu, H.; Yang, Y.; Xiao, S.; Wang, C.; Russell, T. P.; Cao, Y. Single-Junction Polymer Solar Cells with High Efficiency and Photovoltage. *Nat. Photonics* **2015**, *9*, 174–179.
4. Yin, Z.; Wei, J.; Zheng, Q. Interfacial Materials for Organic Solar Cells: Recent Advances and Perspectives. *Adv. Sci.* **2016**, *3*, 1500362.

5. He, Z.; Zhong, C.; Huang, X.; Wong, W.-Y.; Wu, H.; Chen, L.; Su, S.; Cao, Y. Simultaneous Enhancement of Open-Circuit Voltage, Short-Circuit Current Density, and Fill Factor in Polymer Solar Cells. *Adv. Mater.* **2011**, *23*, 4636–4643.
6. Liao, S.-H.; Li, Y.-L.; Jen, T.-H.; Cheng, Y.-S.; Chen, S.-A. Multiple Functionalities of Polyfluorene Grafted with Metal Ion-Intercalated Crown Ether as an Electron Transport Layer for Bulk-Heterojunction Polymer Solar Cells: Optical Interference, Hole Blocking, Interfacial Dipole, and Electron Conduction. *J. Am. Chem. Soc.* **2012**, *134*, 14271–14274.
7. Seo, J. H.; Gutacker, A.; Sun, Y.; Wu, H.; Huang, F.; Cao, Y.; Scherf, U.; Heeger, A. J.; Bazan, G. C. Improved High-Efficiency Organic Solar Cells via Incorporation of a Conjugated Polyelectrolyte Interlayer. *J. Am. Chem. Soc.* **2011**, *133*, 8416–8419.
8. Vasilopoulou, M.; Georgiadou, D. G.; Soultati, A.; Boukos, N.; Gardelis, S.; Palilis, L. C.; Fakis, M.; Skoulatakis, G.; Kennou, S.; Botzakaki, M.; Georga, S.; Krontiras, C. A.; Auras, F.; Fattakhova-Rohlfing, D.; Bein, T.; Papadopoulos, T. A.; Davazoglou, D.; Argitis, P. Atomic-Layer-Deposited Aluminum and Zirconium Oxides for Surface Passivation of TiO_2 in High-Efficiency Organic Photovoltaics. *Adv. Energy Mater.* **2014**, *4*, 1400214.
9. Papageorgiou, A. C.; Beglitis, N. S.; Pang, C. L.; Teobaldi, G.; Cabailh, G.; Chen, Q.; Fisher, A. J.; Hofer, W. A.; Thornton, G. Electron Traps and their Effect on the Surface Chemistry of TiO_2(110). *Proc. Natl. Acad. Sci. USA* **2010**, *107*, 2391–2396.
10. Thambidurai, M.; Kim, J. Y.; Ko, Y.; Song, H.-J.; Shin, H.; Song, J.; Lee, Y.; Muthukumarasamy, N.; Velauthapillai, D.; Lee, C. High-Efficiency Inverted Organic Solar Cells with Polyethylene Oxide-Modified Zn-Doped TiO_2 as an Interfacial Electron Transport Layer. *Nanoscale*, **2014**, *6*, 8585–8589.
11. Xu, M.-F.; Zhu, X.-Z.; Shi, X.-B.; Liang, J.; Jin, Y.; Wang, Z.-K.; Liao, L.-S. Plasmon Resonance Enhanced Optical Absorption in Inverted Polymer/Fullerene Solar Cells with Metal Nanoparticle-Doped Solution-Processable TiO_2 Layer. *ACS Appl. Mater. Interfacials* **2013**, *5*, 2935–2942.
12. Kim, G.; Kong, J.; Kim, J.; Kang, H.; Back, H.; Kim, H.; Lee, K. Overcoming the Light-Soaking Problem in Inverted Polymer Solar Cells by Introducing a Heavily Doped Titanium Sub-Oxide Functional Layer. *Adv. Energy Mater.* **2015**, *5*, 1401298.
13. You, J.; Chen, C.-C.; Dou, L.; Murase, S.; Duan, H-S.; Hawks, S.; Xu, T,; Son, H. J.; Yu, L.; Ynag, Y. Metal oxide nanoparticles as electron-transport layer in high-performance and stable inverted polymer solar cells. *Adv. Mater.* **2012**, *24*, 5267–5272.
14. Lim, F. J.; Krishnamoorthy, A.; Ho, G. W.; Device Stability and Light-Soaking Characteristics of High-Efficiency Benzodithiophene–Thienothiophene Copolymer-Based Inverted Organic Solar Cells with F-TiO_x Electron-Transport Layer. *ACS Appl. Mater. Interfacials* **2015**, *7* (22),12119–12127.
15. Li, Z.; Li, S.; Zhang, Z.; Zhang, X.; Li, J.; Liu, C.; Shen, L.; Guo, W.; Ruan, S. Enhanced Electron Extraction Capability of Polymer Solar Cells via Modifying the Cathode Buffer Layer with Inorganic Quantum Dots. *Phys. Chem. Chem. Phys.* **2016**, *18*, 11435–11442.
16. Li, Z.; Zhang, X.; Liu, C.; Zhang, Z.; Li, J.; Shen, L.; Guo, W.; Ruan, S. Enhanced Electron Extraction Capability of Polymer Solar Cells via Employing Electrostatically Self-Assembled Molecule on Cathode Interfacial Layer. *ACS Appl. Mater. Interfacials* **2016**, *8*, 8224–8231.
17. Sun, C.; Li, X.; Wang, G.; Li, P.; Zhang, W.; Jiu, T.; Jiang, N.; Fang, J. Highly Efficient Inverted Polymer Solar Cells Using Fullerene Derivative Modified TiO2 Nanorods as the Buffer Layer. *RSC Adv.* **2014**, *4*, 19529–19532.
18. Thambidurai, M.q;Kim J. Y.q;Ko, Y.q;Song, H.-J. Shin, H.; Song, J.; Lee, Y.; Muthukumarasamy, N.; Velauthapillai, D; Lee, C. High-efficiency inverted organic solar cells with polyethylene oxide-modified Zn-doped TiO_2 as an interfacial electron transport layer. *Nanoscale* **2014**, *6*, 8585-8589.
19. D. Yang, P. Fu, F. Zhang, N. Wang, J. Zhang, C. Li, High Efficiency Inverted Polymer Solar Cells with Room-Temperature Titanium Oxide/Polyethylenimine Films as Electron Transport Layers. *J. Mater. Chem. A* **2014**, *2*, 17281–17285.
20. Heinrichova, P.; Dzik, P.; Tkacz, J.; Vala, M; Weiter, M. UV-cured TiO_2 electron transport layers for printable solar cell. *RSC Adv.* **2016**, *6*, 66705-66711.
21. Lilliedal, M. R.; Medford, A. J.; Madsen, M. V.; Norrman, K.; Krebs, F. C. The Effect of Post-Processing Treatments on Inflection Points in Current–Voltage Curves of Roll-to-Roll Processed Polymer Photovoltaics. *Sol. Energy Mater. Sol. Cells* **2010**, *94*, 2018–2031.

22. Steim, R.; Choulis, S. A.; Schilinsky, P.; Brabec, C. J. Interfacial Modification for Highly Efficient Organic Photovoltaics. *Appl. Phys. Lett.* **2008**, *92*, 093303.
23. Trost, S.; Zilberberg, K.; Behrendt, A.; Polywka, A.; Görrn, P.; Reckers, P.; Maibach, J.; Mayer, T.; Riedl, T. Overcoming the "Light-Soaking" Issue in Inverted Organic Solar Cells by the Use of Al:ZnO Electron Extraction Layers. *Adv. Energy Mater.* **2013**, *3*, 1437–1444.
24. Trost, S.; Behrendt, A.; Becker, T.; Polywka, A.; Görrn, P.; Riedl, T. Tin Oxide (SnO_x) as Universal "Light-Soaking" Free Electron Extraction Material for Organic Solar Cells *Adv. Energy Mater*. **2015**, *5*, 1500277.
25. Lim, F. J.; Set, Y. T.; Krishnamoorthy, A.; Ouyang, J.; Luther, J.; Ho, G. W. Addressing the Light-soaking Issue in Inverted Organic Solar Cells Using Chemical Bath Deposited Fluorinated TiO_x Electron Transport Layer. *J. Mater. Chem. A* **2015,** *3*, 314-322.
26. Mizuno, N.; Yamaguchi, K.; Kamata, K. Epoxidation of Olefins with Hydrogen Peroxide Catalyzed by Polyoxometalates. *Coord. Chem. Rev.* **2005**, *249*, 1944–1956.
27. Rhule, J. T.; Hill, C. L.; Judd, D. A. Polyoxometalates in Medicine. *Chem. Rev*. **1998**, *98*, 327–358.
28. Pope, M. T.; Müller, A. Polyoxometalate Chemistry: An Old Field with New Dimensions in Several Disciplines. *Angew. Chem., Int. Ed. Engl*. **1991**, *30*, 34–48.
29. Vasilopoulou, M.; Raptis, I.; Argitis, P.; Aspiotis, I.; Davazoglou, D.; Polymeric electrolytes for WO_3-based all solid-state electrochromic displays. *Microelectron. Eng*. **2006**, *83*, 1414–1417.
30. Neumann, R.; Dahan, M. A Ruthenium-Substituted Polyoxometalate as an Inorganic Dioxygenase for Activation of Molecular Oxygen. *Nature* **1997**, *388*, 353–355.
31. Palilis, L. C.; Vasilopoulou, M.; Georgiadou, D. G.; Argitis, P. A Water Soluble Inorganic Molecular Oxide as a Novel Efficient Electron Injection Layer for Hybrid Light-Emitting Diodes (HyLEDs). *Org. Electron.* **2010**, *11*, 887–894.
32. Palilis, L. C.; Vasilopoulou, M.; Douvas, A. M.; Georgiadou, D. G.; Kennou, S.; Stathopoulos, N. A.; Constantoudis, V.; Argitis, P. Solution Processable Tungsten Polyoxometalate as Highly Effective Cathode Interlayer for Improved Efficiency and Stability Polymer Solar Cells. *Sol. Energy Mater. Sol. Cells* **2013**, *114*, 205–213.
33. Vasilopoulou, M.; Douvas, A. M.; Palilis, L. C.; Kennou, S.; Argitis, P. Old Metal Oxide Clusters in New Applications: Spontaneous Reduction of Keggin and Dawson Polyoxometalate Layers by a Metallic Electrode for Improving Efficiency in Organic Optoelectronics. *J. Am. Chem. Soc.* **2015**, *137*, 6844–6856.
34. Vasilopoulou, M.; Polydorou, E.; Douvas, A. M.; Palilis, L. C.; Kennou, S.; Argitis, P. Annealing-Free Highly Crystalline Solution-Processed Molecular Metal Oxides for Efficient Single-Junction and Tandem Polymer Solar Cells. *Energy Environ. Sci.* **2015**, *8*, 2448–2463.
35. Jia, X.; Shen, L.; Yao, M.; Liu, Y.; Yu, W.; Guo, W.; Ruan, S. Highly Efficient Low-Bandgap Polymer Solar Cells with Solution-Processed and Annealing-Free Phosphomolybdic Acid as Hole-Transport Layers. *ACS Appl. Mater. Interfacials* **2015**, ***7***, 5367–5372.
36. Zhu, Y.; Yuan, Z.; Cui, W.; Wu, Z.; Sun, Q.; Wang, S.; Kang, Z.; Sun, B. A Cost-Effective Commercial Soluble Oxide Cluster for Highly Efficient and Stable Organic Solar Cells. *J. Mater. Chem. A* **2014**, *2*, 1436–1442.
37. Alaaeddine, M.; Zhu, Q.; Fichou, D.; Izzet, G.; Rault, J. E.; Barrett, N.; Proust, A.; Tortech, L. Enhancement of Photovoltaic Efficiency by Insertion of a Polyoxometalate Layer at the Anode of an Organic Solar Cell. *Inorg. Chem. Front.* **2014**, *1*, 682–688.
38. Tountas, M.; Topal, Y.; Kus, M.; Ersöz, M.; Fakis, M.; Argitis, P.; Vasilopoulou, M. Water-Soluble Lacunary Polyoxometalates with Excellent Electron Mobilities and Hole Blocking Capabilities for High Efficiency Fluorescent and Phosphorescent Organic Light Emitting Diodes. *Adv. Funct. Mater.* **2016**, *26*, 2655–2665.
39. Song, S.; Moon, B. J.; Hörantner, M. T.; Lim, J.; Kang, G.; Park, M.; Kim, J. Y.; Snaith, H. J.; Park, T. Interfacial Electron Accumulation for Efficient Homo-Junction Perovskite Solar Cells. *Nano Energy* **2016**, *28*, 269-276.
40. Guo, S.; Cao, B.; Wang, W.; Moulin, J.-F.; Müller-Buschbaum, P. Effect of Alcohol Treatment on the Performance of PTB7:PC_{71}BM Bulk Heterojunction Solar Cells. *ACS Appl. Mater. Interfaces* **2015**, *7*, 4641-4649.

41. Ju, H.; Knesting, K. M.; Zhang, W.; Pan, X.; Wang, C.-H.; Yang, Y.-W.; Ginger, D. S.; Zhu, J. Interplay between Interfacial Structures and Device Performance in Organic Solar Cells: A Case Study with the Low Work Function Metal, Calcium. *ACS Appl. Mater. Interfaces*, **2016**, *8* (3), 2125–2131.
42. Papadopoulos, T. A.; Li, H.; Kim, E.-G.; Liu, J.; Cella, J. A.; Heller, C. M.; Shu, A.; Kahn, A.; Duggal, A.; Brédas, J.-L. Impact of Functionalized Polystyrenes as the Electron Injection Layer on Gold and Aluminum Surfaces: A Combined Theoretical and Experimental Study. *Isr. J. Chem.* **2014**, *54*, 779–788.
43. Cowan, S. R.; Roy, A.; Heeger, A. J. Recombination in Polymer-Fullerene Bulk Heterojunction Solar Cells. *Phys. Rev. B* **2010**, *82*, 245207.
44. Maurano, A.; Hamilton, R.; Shuttle, C. G.; Ballantyne, A. M.; Nelson, J.; O'Regan, B.; Zhang, W.; McCulloch, I.; Azimi, H.; Morana, M.; Brabec, C. J.; Durrant, J. R. Recombination Dynamics as a Key Determinant of Open Circuit Voltage in Organic Bulk Heterojunction Solar Cells: A Comparison of Four Different Donor Polymers. *Adv. Mater.* **2010**, *22*, 4987–4992.
45. Hawks, S. A.; Deledalle, F.; Yao, J.; Rebois, D. G.; Li, G.; Nelson, J.; Yang, Y.; Kirchartz, T.; Durrant, J. R. Relating Recombination, Density of States, and Device Performance in an Efficient Polymer:Fullerene Organic Solar Cell Blend. *Adv. Energy Mater.* **2013**, *3*, 1201–1209.
46. Ruderer, M. A.; Guo, S.; Meier, R.; Chiang, H.-Y.; Körstgens, V.; Wiedersich, J.; Perlich, J.; Roth, S. V.; Müller-Buschbaum, P. Solvent-Induced Morphology in Polymer-Based Systems for Organic Photovoltaics. *Adv. Funct. Mater.* **2011**, *21*, 3382-3391.
47. Reinhardt, J.; Grein, M.; Buhler, C.; Schubert, M.; Wurfel, U. Identifying the Impact of Surface Recombination at Electrodes in Organic Solar Cells by Means of Electroluminescence and Modeling. *Adv. Energy Mater*. **2014**, *5*, 1400081.
48. Wurfel, U.; Neher, D.; Spies,A.; Albrech, S. Impact of charge transport on current–voltage characteristics and power-conversion efficiency of organic solar cells. *Nat Commun*. **2015**; *6*, 6951.
49. Scharber, M. C. On the Efficiency Limit of Conjugated Polymer:Fullerene-Based Bulk Heterojunction Solar Cells. *Adv. Mater***. 2016**, *28*, 1994-2001.
50. Wang, K.; Liu, C.; Meng, T.; Yi, C.; Gong, X. Inverted Organic Photovoltaic Cells. *Chem. Soc. Rev*. **2016**, *45*, 2937–2975.
51. Yin, Z.; Zheng, Q.; Chen, S.-C.; Li, J. Cai, D.; Ma, Y.; Wei, J. Solution-Derived Poly(ethylene glycol)-TiO_x Nanocomposite Film as a Universal Cathode Buffer Layer for Enhancing Efficiency and Stability of Polymer Solar Cells. *Nano Res.* **2015**, *8*, 456–468.
52. Nian, L.; Zhang, W.; Zhu, N.; Liu, L.; Xie, Z.; Wu, H.; Würthner, F.; Ma, Y. Photoconductive Cathode Interlayer for Highly Efficient Inverted Polymer Solar Cells. *J. Am. Chem. Soc.* **2015**, *137*, 6995–6998.
53. Nian, L.; Zhang, W.; Wu, S.; Qin, L.; Liu, L.; Xie, Z.; Wu, H.; Ma, Y. Perylene Bisimide as a Promising Zinc Oxide Surface Modifier: Enhanced Interfacial Combination for Highly Efficient Inverted Polymer Solar Cells. *ACS Appl. Mater. Interfaces* **2015**, *7*, 25821–25827.
54. Nian, L.; Gao, K; Liu, F.; Kan, Y.; Jiang, X.; Liu, L.; Xie, Z.; Peng, X.; Russell, T. P.; Ma, Y. 11% Efficient Ternary Organic Solar Cells with High Composition Tolerance via Integrated Near-IR Sensitization and Interface Engineering. *Adv. Mater.* **2016**, DOI: 10.1002/adma.201602834.
55. Yin, Z.; Wei, J.; Zheng, Q. Interfacial Materials for Organic Solar Cells: Recent Advances and Perspectives. *Adv. Sci.* **2016**, 1500362, DOI: 10.1002/advs.201500362.
56. Cowan, S. R.; Roy, A.; Heeger, A. J. Recombination in Polymer-Fullerene Bulk Heterojunction Solar Cells. *Phys. Rev. B* **2010**, *82*, 245207.
57. Maurano, A.; Hamilton, R.; Shuttle, C. G.; Ballantyne, A. M.; Nelson, J.; O'Regan, B.; Zhang, W.; McCulloch, I.; Azimi, H.; Morana, M.; Brabec, C. J.; Durrant, J. R. Recombination Dynamics as a Key Determinant of Open Circuit Voltage in Organic Bulk Heterojunction Solar Cells: A Comparison of Four Different Donor Polymers. *Adv. Mater.* **2010**, *22*, 4987–4992.
58. Hawks, S. A.; Deledalle, F.; Yao, J.; Rebois, D. G.; Li, G.; Nelson, J.; Yang, Y.; Kirchartz, T.; Durrant, J. R. Relating Recombination, Density of States, and Device Performance in an Efficient Polymer:Fullerene Organic Solar Cell Blend. *Adv. Energy Mater.* **2013**, *3*, 1201–1209.
59. Ruderer, M. A.; Müller-Buschbaum, P. Morphology of Polymer-based Bulk Heterojunction Films for Organic Photovoltaics. *Soft Matter* **2011**, *7*, 5482-5493.
60. Chen, W.; Nikiforov, M. P.; Darling, S. B. Morphology Characterization in Organic and Hybrid Solar Cells. *Energy Environ. Sci*. **2012**, *5*, 8045-8074.

61. Mariano Campoy-Quiles, Ferenczi,T.; Agostinelli, T.; Etchegoin, P. G.; Kim, Y. Anthopoulos, T. D.; Stavrinou, P. N.; Bradley, D. D. C.; Nelson, J. Morphology evolution via self-organization and lateral and vertical diffusion in polymer:fullerene solar cell blends. *Nat. Mater*. **2008,** *7*, 158-164.
62. Roehling, J. D.; Baran, D.; Sit, J.; Kassar, T.; Ameri, T.; Unruh, T.; Brabec, C. J.; Moulé., A. J. Nanoscale Morphology of PTB7 Based Organic Photovoltaics as a Function of Fullerene Size. *Sci. Rep.* **2016**, *6*, 30915.
63. Liu, F.; Zhao,W.; Tumbleston,J. R.; Wang, C.; Gu, Y.; Wang, D.; Briseno, A.L.; Ade, H.; Russell, P. Understanding the Morphology of PTB7:PCBM Blends in Organic Photovoltaics. *Adv. Energy Mater*. **2014**, *2*, 1301377.
64. Nisar, A.; Wang, X. Surfactant-encapsulated polyoxometalate building blocks: controlled assembly and their catalytic properties. Dalton Transactions. *Dalton Trans.* **2012**,*41*, 9832-9845.
65. Ding, Z.; Kettle, J.; Horie, M.; Chang, S. W.; Smith, G. C.; Shames, A. I.; Katz, E. A. Efficient solar cells are more stable: the impact of polymer molecular weight on performance of organic photovoltaics. *J. Mater. Chem*. A **2016**, *4*, 7274-7280.
66. Li, W.; Zhang, W.; Van Reenen, S.; Sutton, R. J.; Fan, J.; Haghighirad, A. A.; Johnston, M. B.; Wang, L.; Snaith, H. J. Enhanced UV-Light Stability of Planar Heterojunction Perovskite Solar Cells with Caesium Bromide Interface Modification. *Energy Environ. Sci.* **2016**, *9*, 490–498.
67. Jeong, J.; Seo, J.; Nam, S.; Han, H.; Kim, H.; Anthopoulos, T. D.; Bradley, D. D. C.; Kim, Y. Significant Stability Enhancement in High-Efficiency Polymer:Fullerene Bulk Heterojunction Solar Cells by Blocking Ultraviolet Photons from Solar Light. *Adv.Sci*. **2016**, *3*, 1500269.
68. Mizuno, N.; Min, J.-S.; Taguchi, A. Preparation and Characterization of $Cs_{2.8}H_{1.2}PMo_{11}Fe(H_2O)O_{39}\cdot 6H_2O$ and Investigation of Effects of Iron-Substitution on Heterogeneous Oxidative Dehydrogenation of 2-Propanol. *Chem. Mater*. **2004**, *16*, 2819–2825.
69. Li, X.-X.; Fang, W.-H.; Zhao, J.-W; Yang, G.-Y. The First 3-Connected $SrSi_2$-Type 3D Chiral Framework Constructed from $\{Ni_6PW_9\}$ Building Units. *Chem. – Eur. J.* **2015**, *21*, 2315–2318.
70. Kostis, I.; Vourdas, N.; Papadimitropoulos, G.; Douvas, A.; Vasilopoulou, M.; Boukos, N.; Davazoglou, D. Effect of the Oxygen Sub-Stoichiometry and of Hydrogen Insertion on the Formation of Intermediate Bands within the Gap of Disordered Molybdenum Oxide Films. *J. of Phys. Chem. C* **2013**, *117*, 18013-18020.

Tables

Table 1. Performance characteristics of polymer solar cells of inverted architecture: FTO/TiO_2/POM/photoactive layer /MoO_x/Al (mean values and standard deviations were extracted from a batch of 24 independent devices).

ETL	J_{sc} (mA cm^{-2})	V_{oc} (V)	FF	PCE (%)	R_s (Ω cm^2)	R_{sh} (Ω cm^2)
P3HT:$PC_{70}BM$						
TiO_2	9.40 (±0.15)	0.60 (±0.01)	0.58 (±0.01)	3.27 (±0.10)	4.1	1900
T_iO_2/B1-W	10.20 (±0.15)	0.63 (±0.01)	0.63 (±0.01)	4.05 (±0.12)	3.2	2850
T_iO_2/B2-W	10.50 (±0.15)	0.63 (±0.01)	0.64 (±0.01)	4.23 (±0.11)	2.8	3500
TiO_2/B1-Mo	10.60 (±0.15)	0.63 (±0.01)	0.65 (±0.01)	4.34 (±0.12)	2.2	3800
P3HT:$IC_{60}BA$						
TiO_2	9.90 (±0.15)	0.77 (±0.01)	0.65 (±0.01)	4.95 (±0.13)	3.9	1800
T_iO_2/B1-W	10.40 (±0.15)	0.80 (±0.01)	0.69 (±0.01)	5.74 (±0.14)	3.0	2800
T_iO_2/B2-W	10.60 (±0.15)	0.81 (±0.01)	0.70 (±0.01)	6.01 (±0.13)	2.8	3700
TiO_2/B1-Mo	10.80 (±0.15)	0.81 (±0.01)	0.71 (±0.01)	6.21 (±0.14)	2.7	4000
PTB7:$PC_{70}BM$						
TiO_2	14.40 (±0.20)	0.71 (±0.01)	0.65 (±0.01)	6.65 (±0.17)	5.8	1000
T_iO_2/B1W	14.80 (±0.20)	0.74 (±0.01)	0.68 (±0.01)	7.45 (±0.17)	4.0	1800
T_iO_2/B2-W	15.30 (±0.20)	0.75 (±0.01)	0.71 (±0.01)	8.15 (±0.17)	3.6	2100
TiO_2/B1-Mo	15.40 (±0.20)	0.75 (±0.01)	0.72 (±0.01)	8.32 (±0.17)	3.5	2200

Table 2. Fitting parameters, obtained by means of a three-exponential function for P3HT (20 nm thick) films (Excitation wavelength: 410 nm. Detection wavelength: 700 nm.) and of a two-exponential function for PTB7 (40 nm thick) films (Excitation wavelength: 468 nm. Detection wavelength: 790 nm.) deposited on TiO_2 substrates without and with the POM interlayers.

P3HT							
Substrate	**A_1**	**τ_1 (ps)**	**A_2**	**τ_2 (ps)**	**A_3**	**τ_3 (ps)**	**$\langle\tau\rangle$ (ps)**
TiO_2	-	-	0.59	2.41	0.41	24.10	**11.30**
TiO_2/B1-W	0.16	0.32	0.53	3.39	0.31	23.80	**9.20**
TiO_2/B2-W	0.27	0.46	0.47	3.57	0.26	22.80	**7.70**
TiO_2/B1-Mo	0.20	0.25	0.50	2.53	0.30	16.80	**6.34**
PTB7							
Substrate	**A_1**	**τ_1 (ns)**	**A_2**	**τ_2 (ns)**	**A_3**	**τ_3 (ns)**	**$\langle\tau\rangle$ (ns)**
TiO_2	0.83	0.29	0.17	0.65	-	-	**0.35**
TiO_2/B1-W	0.87	0.27	0.13	0.59	-	-	**0.31**
TiO_2/B2-W	0.82	0.30	0.18	0.61	-	-	**0.35**
TiO_2/B1-Mo	0.90	0.29	0.10	0.67	-	-	**0.33**

Figures

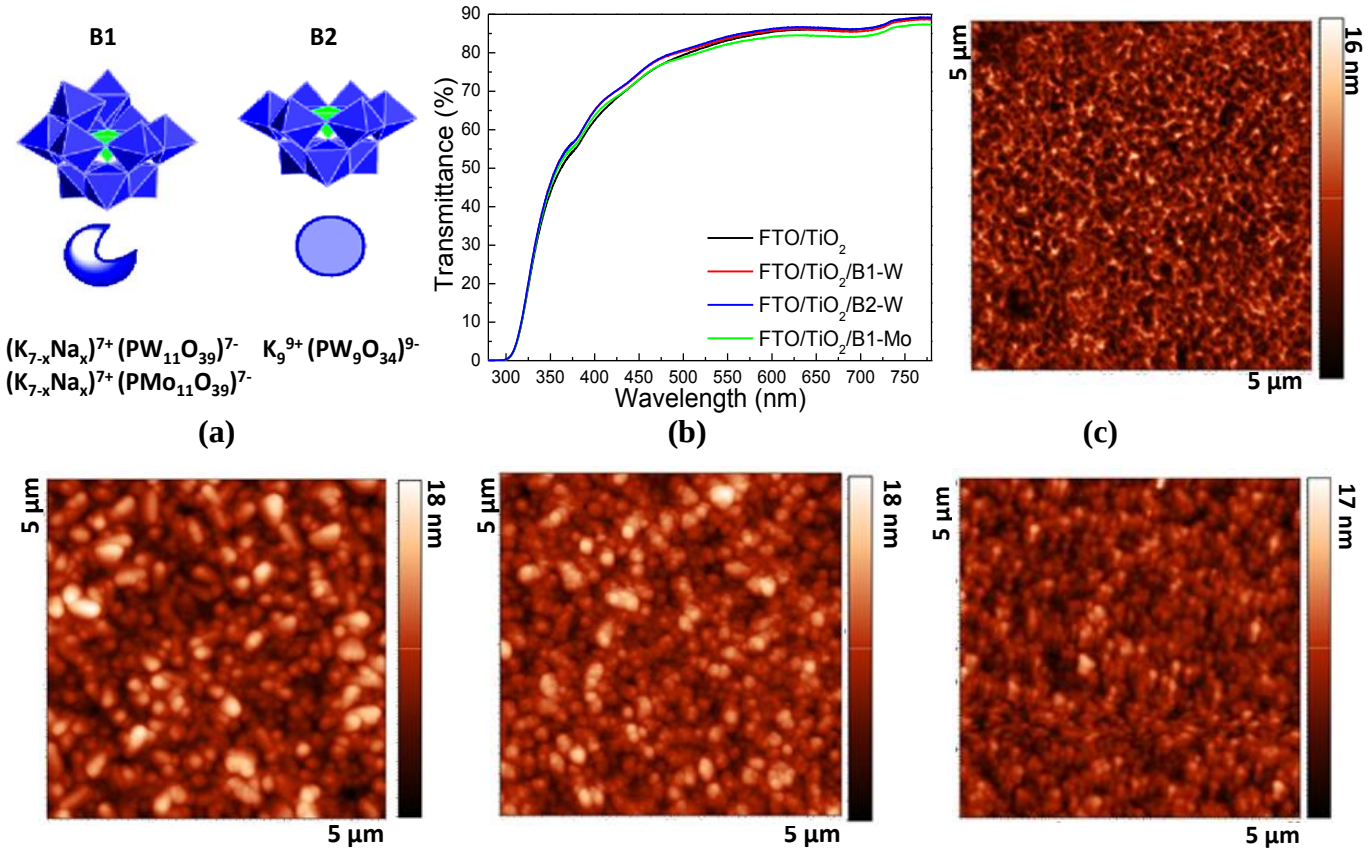

Figure 1 (a) The chemical structures of POMs. (b) Transmittance spectra of TiO_2 films pristine and covered with ~10 nm of POM film. 2D AFM surface topography (5µmx5µm) of (c) TiO_2 film (on glass/FTO substrate) and of ~10 nm (d) B1-W, (e) B2-W and (f) B1-Mo interlayers deposited on TiO_2.

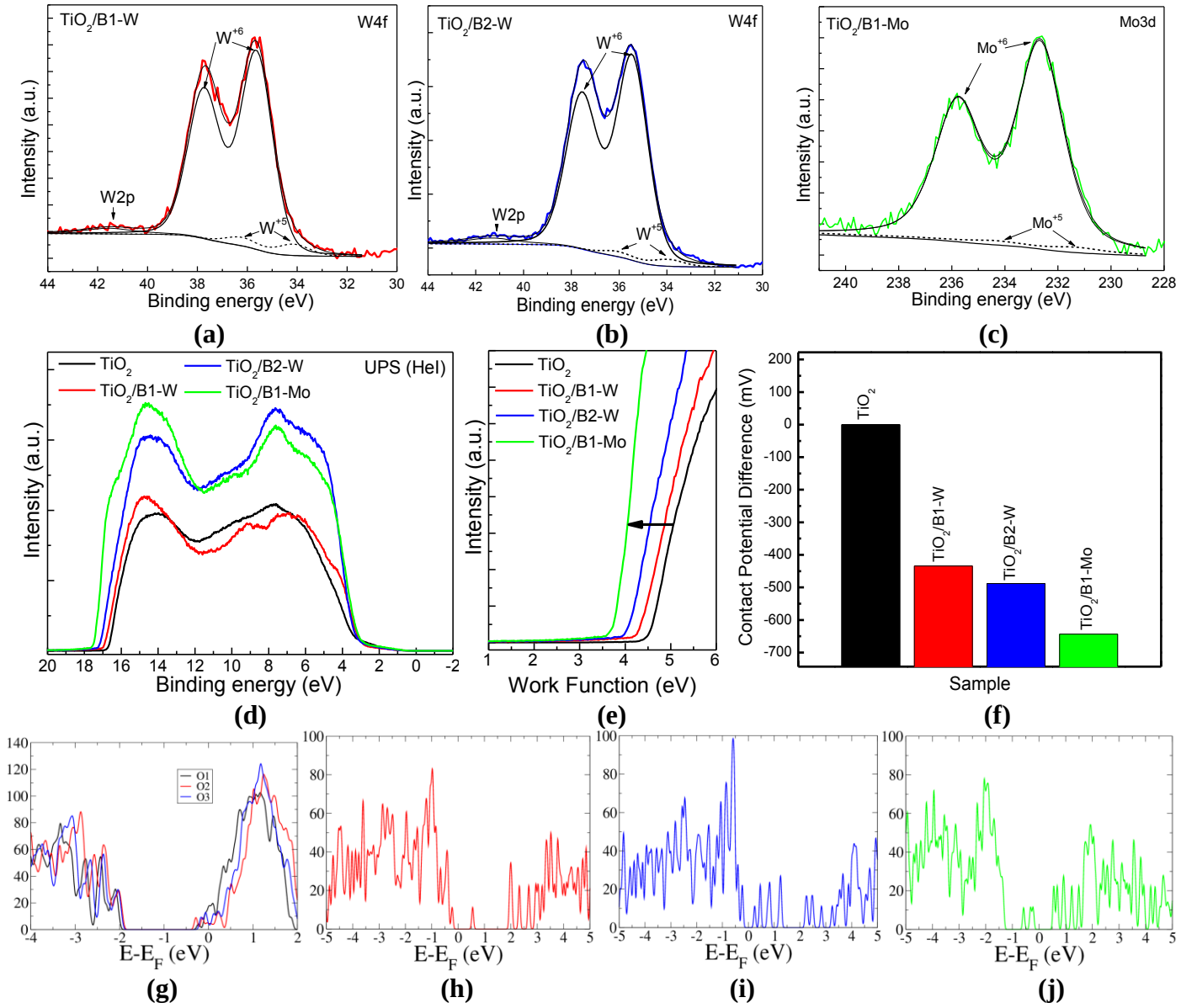

Figure 2 XPS core level peaks of (a) and (b) W 4f and (c) Mo 3d measured on~10 nm B1-W, B2-W and B1-Mo, respectively, spin coated on TiO_x substrates from water solutions with concentrations 10 mg/ml. (d) UPS spectra and (e) the W_F variation as derived from the onset of the high binding energy cut-off region of the same spectra taken on TiO_2 films before and after coating with ~10 nm POM films. (f) Kelvin probe measurements of similar TiO_2 and TiO_2/POM surfaces. The total density of states of (g) TiO_2 (101) surface for each of the three surface oxygen vacancies, O1, O2 and O3, as defined in Ref. 8, (h) B1-W, (i) B2-W, and (j) B1-Mo.

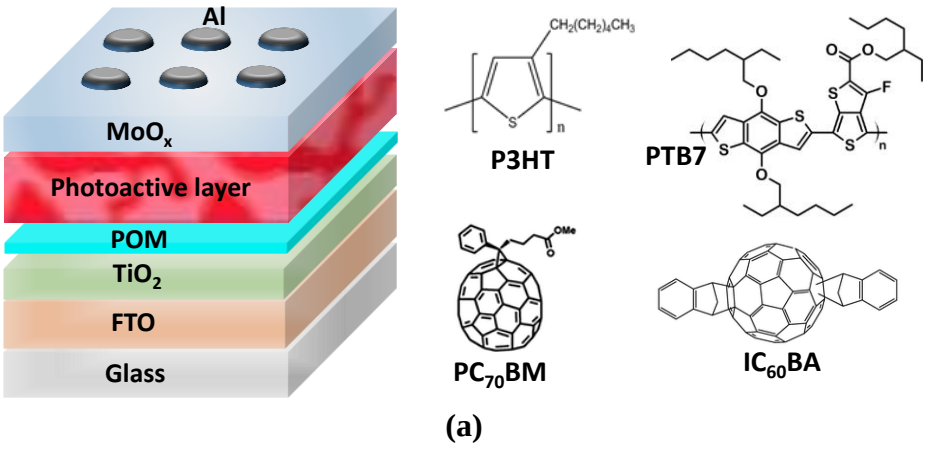

(a)

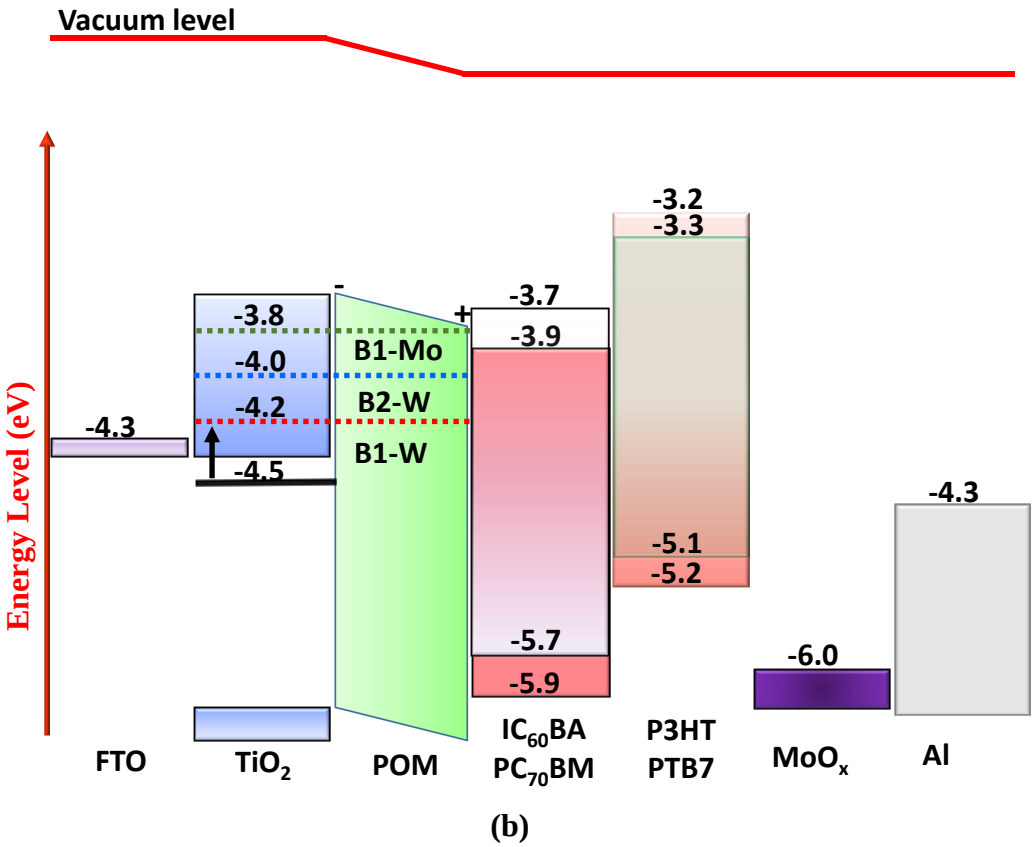

(b)

Figure 3 (a) The inverted polymer solar cell architecture and the chemical structures of organic semiconductors used in this study. (b) Energy level alignment of various interfaces of the inverted devices.

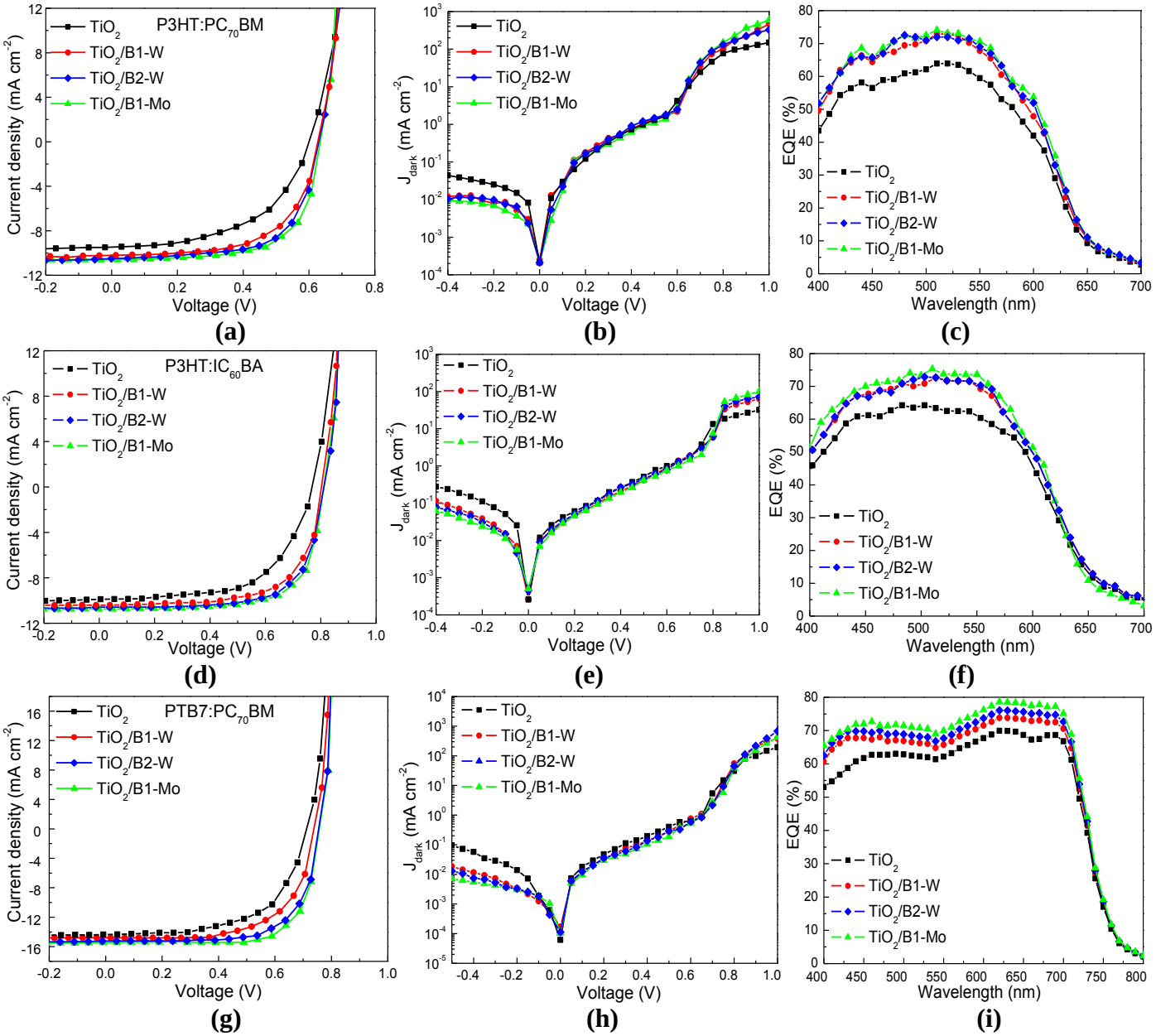

Figure 4 (a), (d), (g) J-V characteristics under AM 1.5G illumination of P3HT:$PC_{70}BM$, P3HT:$IC_{60}BA$ and PTB7:$PC_{70}BM$-based devices fabricated on FTO/TiO_2 substrates without and with ~10 nm POM interfacial layers. (b), (e), (h) The dark J-V characteristics and (c), (f), (i) the EQE measurements of the same devices.

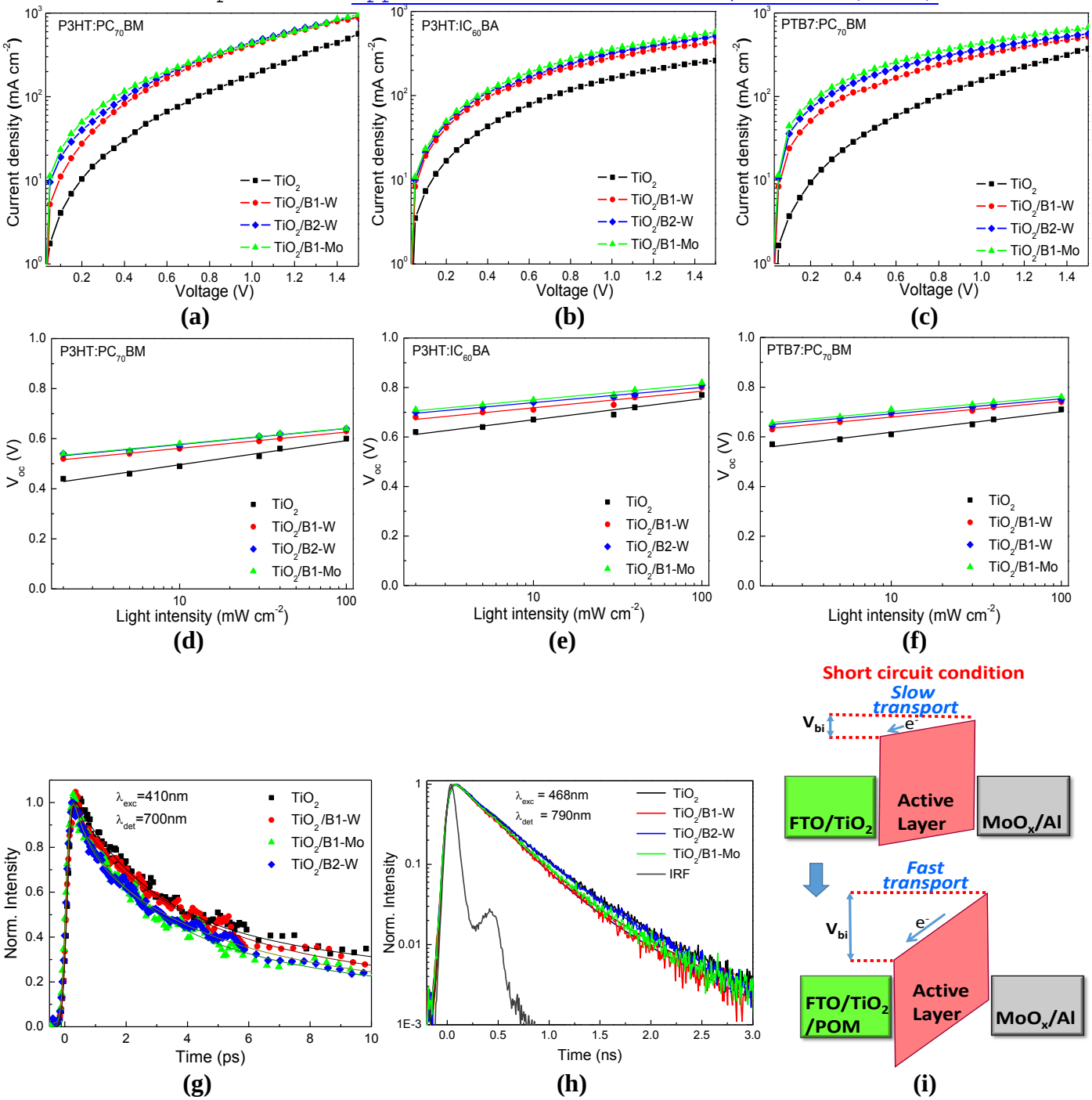

Figure 5 J−V curves (measured in dark) in semi-logarithmic plot obtained in electron-only devices based on (a) P3HT:$PC_{70}BM$, (b) P3HT:$IC_{60}BA$ and (c) PTB7:$PC_{70}BM$ using TiO_2 electron extraction layers before and after the insertion of ~10 nm POM interlayers. Dependence of V_{oc} on 1.5 AM illuminated light intensity of (d) P3HT:$PC_{70}BM$, (e) P3HT:$IC_{60}BA$ and (f) PTB7:$PC_{70}BM$-based polymer solar cells using FTO/TiO_2 substrates without and with ~10 nm POM interlayers. Normalized photoluminescence (PL) dynamics of (g) 20 nm thick P3HT and (h) 40 nm thick PTB7 films deposited on TiO_2 substrates without and with ~10 nm POM interlayers. (i) Expected energy band diagram changes and subsequent faster electron transfer caused by the shifted W_F of TiO_2 layer upon POM modification under short circuit conditions.

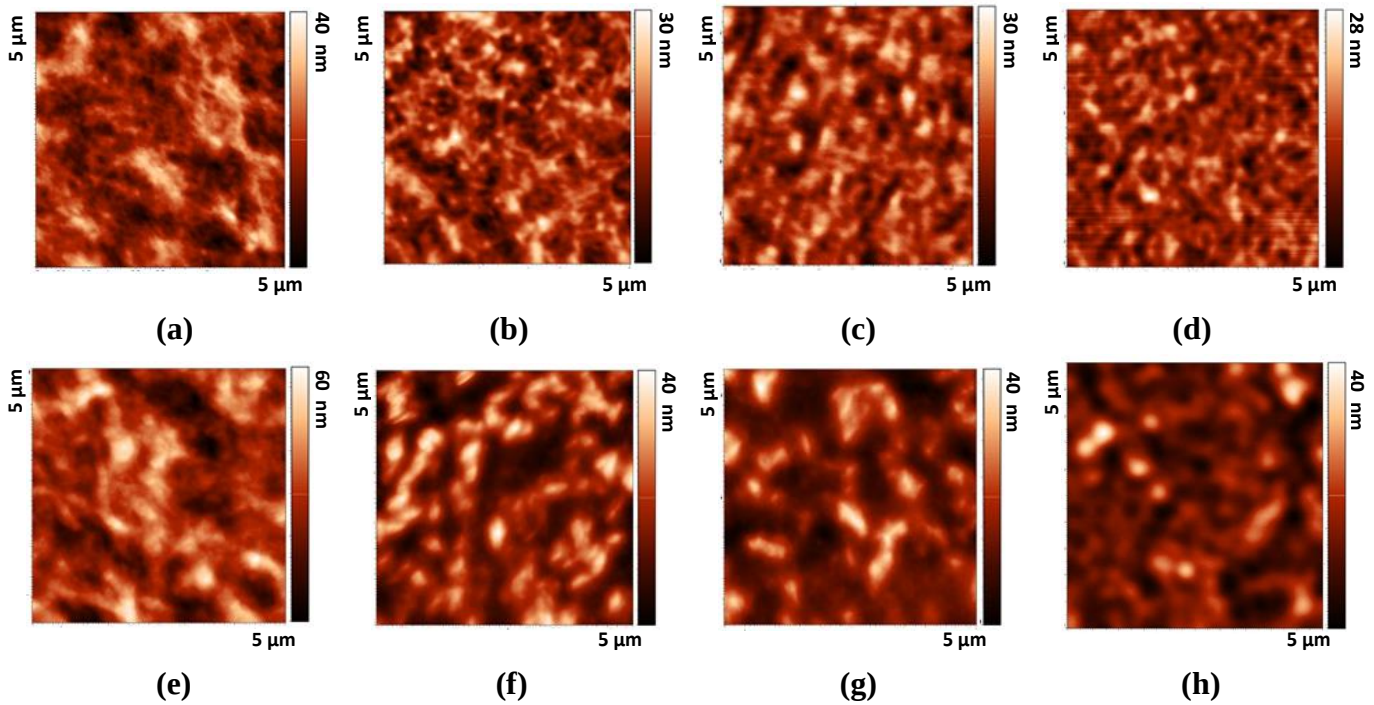

Figure 6 2D AFM surface topography (5µmx5µm) of P3HT:$PC_{70}BM$ films deposited on (a) TiO_2 and on TiO_2 coated with ~10 nm (b) B1-W, (c) B2-W and (d) B1-Mo interlayers. 2D AFM surface topography (5µmx5µm) of P3HT:$IC_{60}BA$ films deposited on (e) TiO_2, (f) TiO_2/B1-W, (g) TiO_2/B2-W and (h) TiO_2/B1-Mo layers.

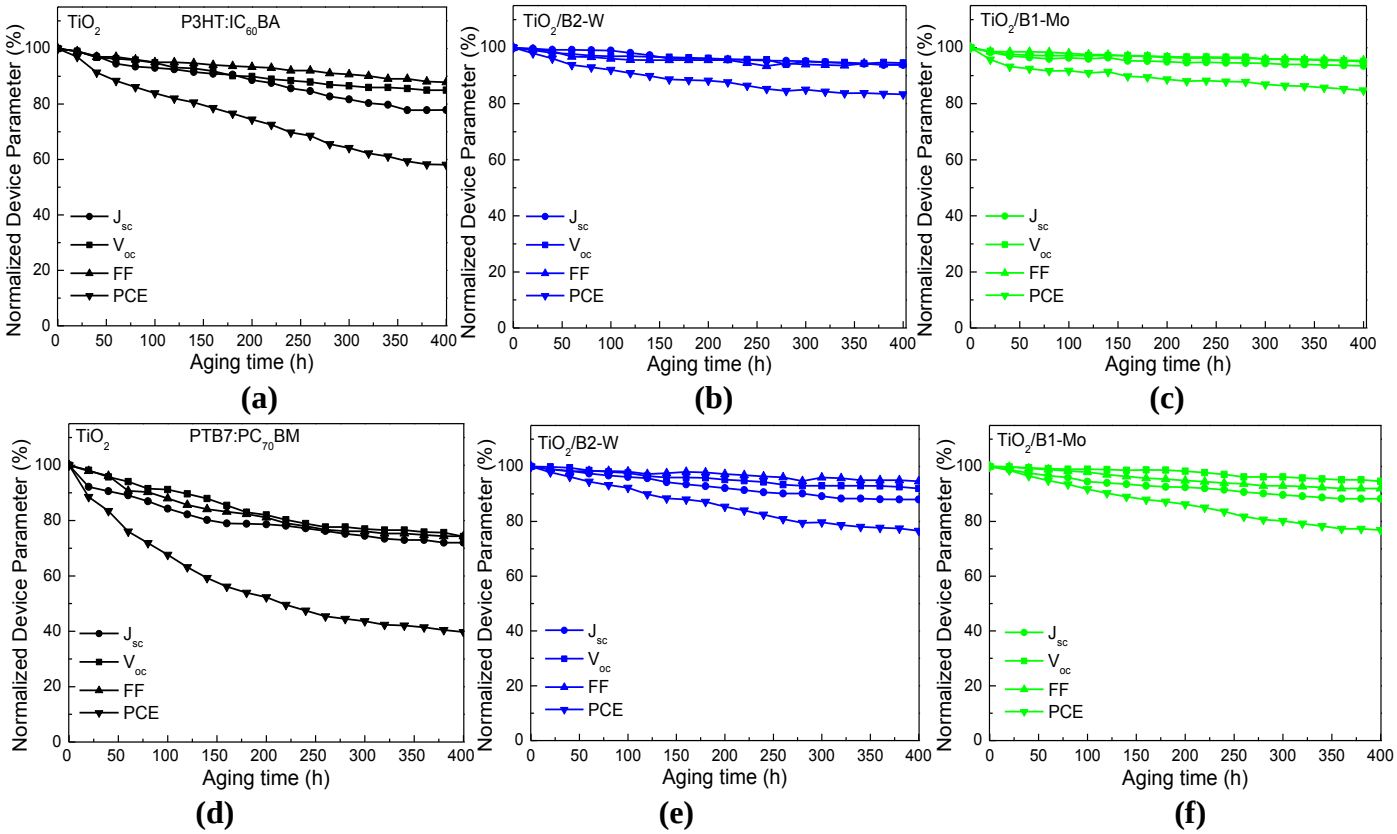

Figure 7 Stability measurements in ambient air: Variation of normalized PCE, J_{sc}, V_{oc} and FF over a period of 400 hours for P3HT:$IC_{60}BA$-based devices using (a) TiO_2, (b) TiO_2/B2-W and (c) TiO_2/B1-Mo electron extraction layers and for PTB7:$PC_{70}BM$-based devices using (d) TiO_2, (e) TiO_2/B2-W and (f) TiO_2/B1-Mo electron extraction layers.

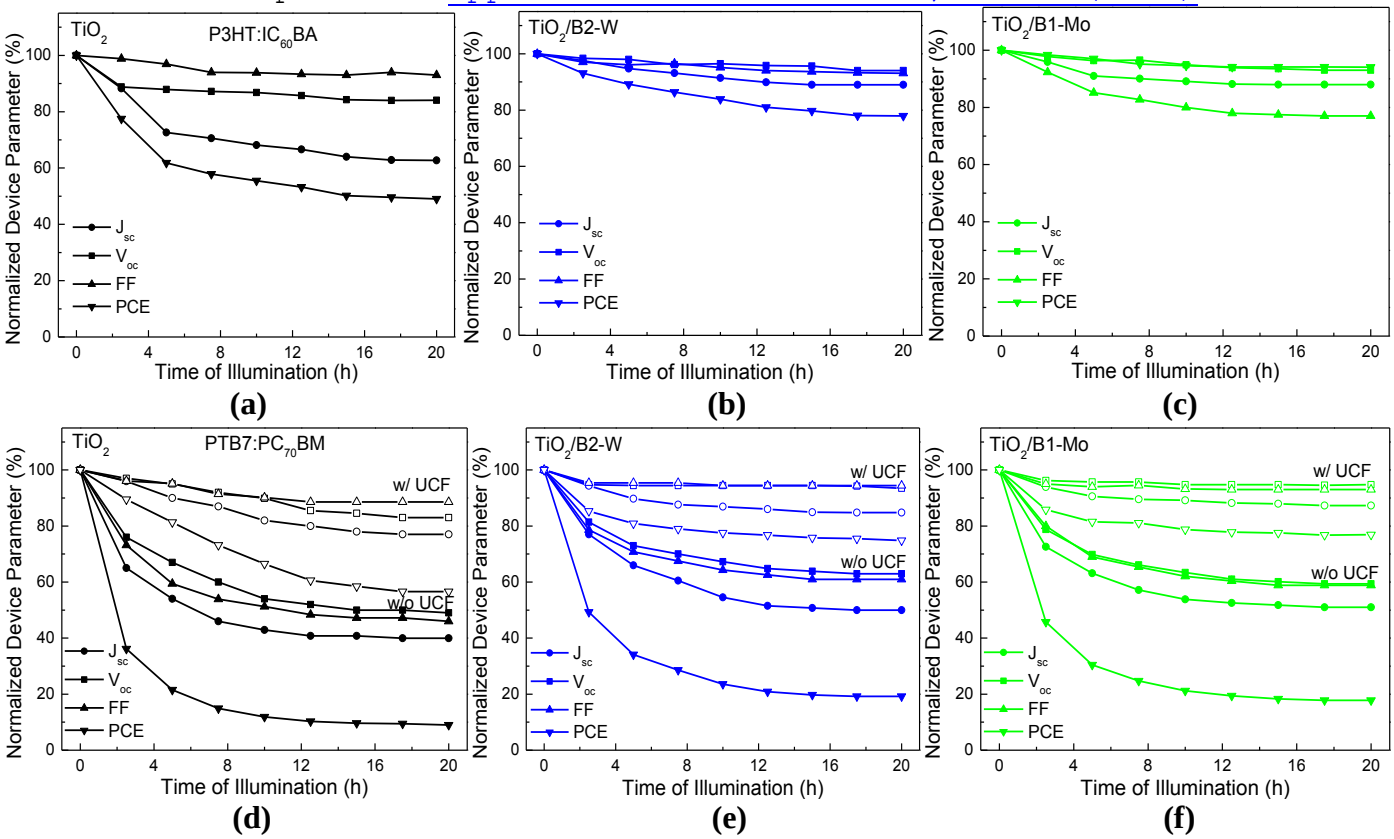

Figure 8 Photostability measurements: Variation of normalized PCE, J_{sc}, V_{oc} and FF as a function of exposure time for 20 h with 1.5 AM simulated light for P3HT:$IC_{60}BA$-based devices using (a) TiO_2, (b) TiO_2/B2-W and (c) TiO_2/B1-Mo electron extraction layers and for PTB7:$PC_{70}BM$-based devices using (d) TiO_2, (e) TiO_2/B2-W and (f) TiO_2/B1-Mo electron extraction layers, illuminated for 20 h with and without the UV cut-off filter (UCF).